JOURNAL OF AIRCRAFT
Vol. 35, No. 5, September–October 1998

Accuracy and Coupling Issues of Aeroelastic Navier–Stokes Solutions on Deforming Meshes

Scott A. Morton,* Reid B. Melville,† and Miguel R. Visbal‡
U.S. Air Force Research Laboratory, Wright–Patterson Air Force Base, Ohio 45433-7913

An implicit time-accurate approach to aeroelastic simulation was developed with particular attention paid to the issues of time accuracy, structural coupling, grid-deformation strategy, and geometric conservation. A Beam–Warming, approximate-factored algorithm, modified to include Newton-like subiterations was coupled with a structural model, also in subiteration form. With a sufficient number of subiterations, this approach becomes a fully implicit, first- or second-order-accurate aeroelastic solver. The solver was used to compute time-accurate solutions of an elastically mounted cylinder. The fully implicit coupling allowed the overall scheme to become second-order accurate in time, significantly reducing the workload for a given accuracy. A new algebraic grid deformation strategy was developed that preserves grid orthogonality near the surface under large deformations. Finally, the oscillatory behavior of an elastically mounted cylinder was reproduced accurately by the present approach, and results compared favorably to previous experiments and simulations.

Nomenclature

b	= half-diameter
C_l, C_d	= lift and drag coefficients
C_p	= static pressure coefficient, $2(p - 1/\gamma M_\infty^2)$
C_x, C_y	= x and y structural damping coefficients
D	= cylinder diameter
E	= total specific energy
$\boldsymbol{F}$, $\boldsymbol{G}$, $\hat{\boldsymbol{F}}$, $\hat{\boldsymbol{G}}$	= flux vectors
$\boldsymbol{H}_{\mathrm{GCL}}$	= geometric conservation law source vector term
I	= identity matrix
J	= Jacobian of coordinate transformation
K_x, K_y	= x and y linear spring coefficients
M_∞	= freestream Mach number
p	= nondimensional static pressure
$\boldsymbol{q}_x$, $\boldsymbol{q}_y$	= components of heat flux vector
Re	= reference Reynolds number, $\rho_\infty u_\infty D/\mu_\infty$
$\boldsymbol{S}$	= structural variables
St	= Strouhal number, fD/u_∞
T	= nondimensional static temperature
t	= transformed time
t^*	= nondimensional time, $u_\infty \bar{t}/D$
$\boldsymbol{U}$, $\hat{\boldsymbol{U}}$	= vector of dependent variables
$\bar{u}$	= reduced velocity
u, v	= nondimensional Cartesian velocity components in x, y directions
x, y	= nondimensional coordinates in streamwise and normal directions
x_{ea}, y_{ea}	= nondimensional coordinates of the cylinder center
$\dot{x}$, $\dot{y}$	= grid velocities
Δt, Δt_s	= time-step sizes
$\Delta \boldsymbol{U}$	= $\boldsymbol{U}^{p+1} - \boldsymbol{U}^p$
δ_{ij}	= Kronecker delta function
δ_ξ, δ_η	= central-difference operators
ζ	= nondimensional structural damping coefficient
μ	= molecular viscosity
μ_s	= mass ratio, $m/\pi\rho_\infty b^2$
ξ, η	= computational coordinates
ξ_t, ξ_x, ξ_y, η_t, η_x, η_y	= metric coefficients of the coordinate transformation
ρ	= nondimensional fluid density
τ_{xx}, τ_{xy}, τ_{yx}, τ_{yy}	= components of viscous stress tensor

Received Feb. 17, 1997; presented as Paper 97-1085 at the AIAA/ASME/ASCE/AHS/ASC 38th Structures, Structural Dynamics, and Materials Conference, Kissimmee, FL, April 7–10, 1997; revision received Feb. 5, 1998; accepted for publication March 15, 1998. This paper is declared a work of the U.S. Government and is not subject to copyright protection in the United States.

*Aerospace Engineer, Aeromechanics Division; currently Assistant Professor, Aeronautics Department, HQ USAFA/DFAN, 2354 Fairchild Drive, Suite 6H27, U.S. Air Force Academy, CO 80840-6222. Senior Member AIAA.

†Aerospace Engineer, Aeromechanics Division. Member AIAA.

‡Technical Area Leader, Aeromechanics Division. Associate Fellow AIAA.

Introduction

An important goal of computational aeroelasticity is to impact the design process with simulations of full aircraft configurations. One challenging aspect of this goal is computing time-accurate aeroelastic solutions in the nonlinear flow regimes associated with transonic conditions, high angle of attack, or maneuvering flight. Although the well-established aeroelastic solvers represent great progress in fluid-structure interaction research, improvements in efficiency and accuracy must be pursued to allow full aircraft time-accurate nonlinear aeroelastic simulations to influence the design cycle.

Historically, researchers interested in dynamic aeroelastic computations have taken well-validated, implicit Navier–Stokes algorithms developed to solve complex flows over three-dimensional, rigid bodies, and extended them to include aeroelastic effects. The most common method of extending these algorithms is to simply lag the effects of moving/deforming structures by one time step,[1–3] allowing current algorithms to be used in updating the aerodynamic variables. After the aerodynamic loads are determined, a structural module is called to update the position and shape of the body. A disadvantage of this strategy is the fact that regardless of the temporal accuracy of the aerodynamic and structural algorithms, the coupling introduces an $\mathcal{O}(\Delta t)$ error for nonstaggered approaches, necessitating small time steps. Overcoming this error requires the coupled scheme to be fully implicit.

One attractive method of converting an alternating direction implicit (ADI) scheme to a fully implicit algorithm is by im-

plementing Newton-like subiterations.[4] Subiterations can eliminate errors from linearization, factorization, lagged boundary conditions, and lagged turbulence models. This strategy is attractive because only minor modifications are made to the baseline solver. The added computational cost of subiterations is typically an additional solution vector storage, and each subiterate is equivalent in workload to a time step of the baseline algorithm. This approach was demonstrated by Rizzetta and Visbal[4] for time-accurate pitching airfoil computations utilizing the k-ε turbulence equations. Stability enhancement was found to be an added benefit of subiteration documented by Rizzetta and Visbal.[4] The current research uses this subiteration methodology to reduce the structural coupling errors and allow higher-order accurate time-integration schemes to be used with relatively minor changes to the baseline aerodynamic solver.

The purpose of the present work is to improve the efficiency of existing coupled Navier–Stokes/structural dynamics algorithms and also to address accuracy issues of dynamic computations on deforming meshes. There are four main issues addressed in the current research: 1) temporal accuracy, 2) structural coupling, 3) grid deformation, and 4) geometric conservation. To reduce the computational resource requirements and limit the flowfield physics to phenomena that are relatively well understood, a two-dimensional aeroelastic circular cylinder is used to analyze these four issues. A circular cylinder is elastically mounted in a freestream with linear springs in both coordinate directions. The aeroelastic cylinder is an attractive model problem for two reasons. First, it displays nonlinear unsteady flowfield physics associated with separation and vortex shedding, and secondly there is both numerical and experimental data available for comparison.[5–7]

A first- and second-order temporally accurate Beam–Warming algorithm with Newton subiteration is used to compute the flowfield. The first two issues of temporal accuracy and coupling are addressed by time-step and maximum subiterate number studies. The issue of geometric conservation is addressed by assessing freestream preservation for large grid deformations. In addition, grid quality is assessed for two grid-deformation strategies. Finally, verification of the overall method's accuracy is obtained through comparison with numerical and experimental solutions in the open literature.

Method of Solution

In this section the aerodynamic governing equations and boundary conditions as well as the structural governing equations are presented.

Aerodynamic Governing Equations

The aerodynamic governing equations are the unsteady compressible two-dimensional Navier–Stokes equations written in nondimensional strong-conservation law form employing a general time-dependent transformation of the form

$$\xi = \xi(x, y, t^*), \qquad \eta = \eta(x, y, t^*), \qquad t = t^* \tag{1}$$

The resulting system of governing equations is expressed as

$$\frac{\partial \hat{\boldsymbol{U}}}{\partial t} + \frac{\partial}{\partial \xi}\left(\hat{\boldsymbol{F}} - \frac{1}{Re}\hat{\boldsymbol{F}}_v\right) + \frac{\partial}{\partial \eta}\left(\hat{\boldsymbol{G}} - \frac{1}{Re}\hat{\boldsymbol{G}}_v\right) = \boldsymbol{H}_{\mathrm{GCL}} \tag{2}$$

$\boldsymbol{H}_{\mathrm{GCL}}$ is a term to enforce the geometric conservation law (GCL) for moving meshes. This term is defined

$$\boldsymbol{H}_{\mathrm{GCL}} = \boldsymbol{U}\left[\frac{\partial J^{-1}}{\partial t} + \left(\frac{\xi_t}{J}\right)_\xi + \left(\frac{\eta_t}{J}\right)_\eta\right] \tag{3}$$

A discussion and derivation of this term is provided in the following section.

Vector quantities appearing in Eq. (2) are defined as

$$\hat{\boldsymbol{U}} = (1/J)\boldsymbol{U} \tag{4}$$

$$\begin{aligned}\hat{\boldsymbol{F}} &= (1/J)(\xi_t \boldsymbol{U} + \xi_x \boldsymbol{F} + \xi_y \boldsymbol{G})\\ \hat{\boldsymbol{G}} &= (1/J)(\eta_t \boldsymbol{U} + \eta_x \boldsymbol{F} + \eta_y \boldsymbol{G})\end{aligned} \tag{5}$$

$$\begin{aligned}\hat{\boldsymbol{F}}_v &= (1/J)(\xi_x \boldsymbol{F}_v + \xi_y \boldsymbol{G}_v)\\ \hat{\boldsymbol{G}}_v &= (1/J)(\eta_x \boldsymbol{F}_v + \eta_y G_v)\end{aligned} \tag{6}$$

With this formulation, the vector of dependent variables $\boldsymbol{U}$ and the flux vectors are given as

$$\boldsymbol{U} = \begin{bmatrix}\rho\\ \rho u\\ \rho v\\ \rho E\end{bmatrix}, \quad \boldsymbol{F} = \begin{bmatrix}\rho u\\ \rho u^2 + p\\ \rho uv\\ (\rho E + p)u\end{bmatrix}, \quad \boldsymbol{G} = \begin{bmatrix}\rho v\\ \rho uv\\ \rho v^2 + p\\ (\rho E + p)v\end{bmatrix} \tag{7}$$

$$\boldsymbol{F}_v = \begin{bmatrix}0\\ \tau_{xx}\\ \tau_{xy}\\ u\tau_{xx} + v\tau_{xy} - q_x\end{bmatrix}, \quad \boldsymbol{G}_v = \begin{bmatrix}0\\ \tau_{yx}\\ \tau_{yy}\\ u\tau_{yx} + v\tau_{yy} - q_y\end{bmatrix} \tag{8}$$

where

$$E = [T/(\gamma - 1)M_\infty^2] + (u^2 + v^2)/2 \tag{9}$$

All variables have been normalized by their representative freestream values except for p that has been nondimensionalized by $\rho_\infty u_\infty^2$. Components of the stress tensor and heat flux vector may be expressed as

$$\tau_{x_i x_j} = \mu\left(\frac{\partial u_i}{\partial x_j} + \frac{\partial u_j}{\partial x_i} - \frac{2}{3}\delta_{ij}\frac{\partial u_k}{\partial x_k}\right) \tag{10}$$

$$q_{x_i} = -\left[\frac{1}{(\gamma - 1)M_\infty^2}\right]\left(\frac{\mu}{Pr}\right)\frac{\partial T}{\partial x_i} \tag{11}$$

where $u_1, u_2 = u, v$, and $x_1, x_2 = x, y$. Sutherland's law for the molecular viscosity coefficient μ and the perfect gas relationship

$$p = \rho T/\gamma M_\infty^2 \tag{12}$$

are also employed, and Stokes' hypothesis for the bulk viscosity coefficient is assumed.

Geometric Conservation Law

This section describes the relationship between the governing equations and the geometric conservation law. The nondimensional Cartesian governing equations can be expressed

$$\frac{\partial \boldsymbol{U}}{\partial t^*} + \frac{\partial}{\partial x}\left(\boldsymbol{F} - \frac{1}{Re}\boldsymbol{F}_v\right) + \frac{\partial}{\partial y}\left(\boldsymbol{G} - \frac{1}{Re}\boldsymbol{G}_v\right) = 0 \tag{13}$$

Using the chain-rule differentiation expressions

$$\frac{\partial(\cdot)}{\partial t^*} = \frac{\partial(\cdot)}{\partial t} + \xi_t\frac{\partial(\cdot)}{\partial \xi} + \eta_t\frac{\partial(\cdot)}{\partial \eta} \tag{14}$$

$$\frac{\partial(\cdot)}{\partial x} = \xi_x\frac{\partial(\cdot)}{\partial \xi} + \eta_x\frac{\partial(\cdot)}{\partial \eta}, \qquad \frac{\partial(\cdot)}{\partial y} = \xi_y\frac{\partial(\cdot)}{\partial \xi} + \eta_y\frac{\partial(\cdot)}{\partial \eta} \tag{15}$$

and premultiplying by the inverse of the transformation Jacobian J, Eq. (13) becomes

$$\begin{aligned}&\frac{\partial \hat{\boldsymbol{U}}}{\partial t} + \frac{\partial}{\partial \xi}\left(\hat{\boldsymbol{F}} - \frac{1}{Re}\hat{\boldsymbol{F}}_v\right) + \frac{\partial}{\partial \eta}\left(\hat{\boldsymbol{G}} - \frac{1}{Re}\hat{\boldsymbol{G}}_v\right)\\ &\quad = \boldsymbol{U}\left[\frac{\partial J^{-1}}{\partial t} + \left(\frac{\xi_t}{J}\right)_\xi + \left(\frac{\eta_t}{J}\right)_\eta\right] + \left(\boldsymbol{F} - \frac{1}{Re}\boldsymbol{F}_v\right)\\ &\quad\times\left[\left(\frac{\xi_x}{J}\right)_\xi + \left(\frac{\eta_x}{J}\right)_\eta\right] + \left(\boldsymbol{G} - \frac{1}{Re}\boldsymbol{G}_v\right)\left[\left(\frac{\xi_y}{J}\right)_\xi + \left(\frac{\eta_y}{J}\right)_\eta\right]\end{aligned} \tag{16}$$

All three terms on the right-hand side (RHS) of Eq. (16) vanish analytically. The difficulty arises when discrete representations of the temporal and spatial derivatives are used. The discrete form of the last two terms are zero when central differences are used for all metric calculations in two dimensions. Unfortunately, this is not true for the first term because of the mixed temporal and spatial derivatives. The first term set to zero is referred to in the literature as the geometric conservation law.[8] The most straightforward approach of accounting for this term is to simply include it in the discrete governing equations, more accurately representing the nontransformed governing equations.

Aerodynamic Boundary Conditions

Numerical boundary conditions for the cylinder provide the connection between aerodynamic equations and structural equations. At the airfoil surface, the no-slip condition requires that

$$u = \dot{x}_b, \qquad v = \dot{y}_b \tag{17}$$

where $\dot{x}_b$ and $\dot{y}_b$ denote the velocity of the moving boundary, with $\dot{x}_b = \dot{y}_b = 0$ in the static case.

The remaining two conditions are the adiabatic wall condition and the inviscid normal momentum equation

$$\frac{\partial T}{\partial \eta} = 0, \qquad \frac{\partial p}{\partial \eta} = -\left(\frac{\rho}{\eta_x^2 + \eta_y^2}\right)(\eta_x \ddot{x}_b + \eta_y \ddot{y}_b) \tag{18}$$

Along the inflow portion of the outer boundary all dependent variables are assigned their respective freestream values. On the outflow boundary, pressure is assigned to be the freestream pressure, whereas first-order accurate extrapolation of all other dependent variables is employed, corresponding to the condition

$$\frac{\partial \boldsymbol{U}}{\partial x} = 0 \tag{19}$$

Periodic conditions for the O-grid are applied at the leading edge of the cylinder, which is facilitated by constructing an overlap of five ξ = const grid lines to preserve the continuity of numerical damping.

Structural Dynamic Governing Equations

The structural model is depicted in Fig. 1. The cylinder is assumed to be constrained to move along the vertical and horizontal inertial directions without rotation. The stiffnesses in the horizontal and vertical directions are modeled by linear springs with structural damping. The current computations assume there is no preferred direction of motion and, therefore, $K_x = K_y$ and $C_x = C_y$.

The governing equations for the two-degrees-of-freedom model[5,7] in dimensional form are

$$m\ddot{x}_{ea} + C_x\dot{x}_{ea} + K_x x_{ea} = \mathcal{D} \tag{20}$$

$$m\ddot{y}_{ea} + C_y\dot{y}_{ea} + K_y y_{ea} = \mathcal{L} \tag{21}$$

where m, $\mathcal{D}$, and $\mathcal{L}$ are the mass, drag, and lift per unit span, respectively. Equations (20) and (21) are nondimensionalized by the aerodynamic scales previously mentioned, yielding

$$\ddot{x}_{ea} + 2\zeta\left(\frac{2}{\bar{u}}\right)\dot{x}_{ea} + \left(\frac{2}{\bar{u}}\right)^2 x_{ea} = \frac{2}{\mu_s \pi} C_d \tag{22}$$

$$\ddot{y}_{ea} + 2\zeta\left(\frac{2}{\bar{u}}\right)\dot{y}_{ea} + \left(\frac{2}{\bar{u}}\right)^2 y_{ea} = \frac{2}{\mu_s \pi} C_l \tag{23}$$

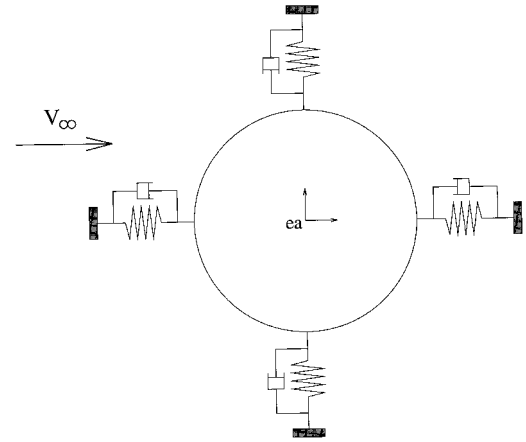

Fig. 1 Aeroelastic cylinder model.

where the following definitions are used

$$\bar{u} = u_\infty / b\omega, \qquad \omega = \omega_{x_y} = \sqrt{K_{x_y}/m} \tag{24}$$

$$\mu_s = m/\pi\rho_\infty b^2, \qquad \zeta = \zeta_{x_y} = C_{x_y}/2\sqrt{mK_{x_y}} \tag{25}$$

Equations (22) and (23) may be cast as a system of first-order ordinary differential equations. Introducing the new variables $s_1 = x_{ea}$, $s_3 = y_{ea}$, $\dot{s}_1 = s_2$ and $\dot{s}_3 = s_4$, the structural equations [(22) and (23)] may be rewritten in matrix form as

$$\frac{\partial \boldsymbol{S}}{\partial t} + \boldsymbol{K}(\boldsymbol{S};\, C_l,\, C_d) = 0, \qquad \boldsymbol{K} = M^{-1}K\boldsymbol{S} - M^{-1}\boldsymbol{Q} \tag{26}$$

$$\boldsymbol{S} = \begin{bmatrix} s_1 \\ s_2 \\ s_3 \\ s_4 \end{bmatrix}, \quad M = \begin{bmatrix} 1 & 0 & 0 & 0 \\ 0 & 1 & 0 & 0 \\ 0 & 0 & 1 & 0 \\ 0 & 0 & 0 & 1 \end{bmatrix}, \quad \boldsymbol{Q} = \begin{bmatrix} 0 \\ \dfrac{2}{\mu_s\pi} C_d \\ 0 \\ \dfrac{2}{\mu_s\pi} C_l \end{bmatrix} \tag{27}$$

$$K = \begin{bmatrix} 0 & -1 & 0 & 0 \\ \left(\dfrac{2}{\bar{u}}\right)^2 & 2\zeta\left(\dfrac{2}{\bar{u}}\right) & 0 & 0 \\ 0 & 0 & 0 & -1 \\ 0 & 0 & \left(\dfrac{2}{\bar{u}}\right)^2 & 2\zeta\left(\dfrac{2}{\bar{u}}\right) \end{bmatrix} \tag{28}$$

Although the mass matrix M is trivial in this case, it is included for generality. Initial conditions for the structural variables are specified to be the static position of the cylinder center and null velocities of the center of the cylinder.

Numerical Procedure

This section describes the numerical procedure for time integration of the aerodynamic equations, as well as the structural dynamic equations. Also, the grid deformation strategy is described.

Time Integration Scheme

Solutions to Eq. (2) are obtained numerically using the implicit approximately factored finite difference algorithm of Beam and Warming,[9] employing a Newton-like subiteration procedure.[4] The numerical algorithm is obtained from Eq. (2) by utilizing either a two- or three-point backward time differencing and linearizing about the solution at subiteration level

p. The choice of first- or second-order temporal accuracy is retained in the following iterative approach by specifying either $\phi = 0$ or $\phi = \frac{1}{2}$, respectively. The numerical algorithm is written in delta form as

$$\left[IJ^{-1} + \phi^i \Delta t_s \delta_\xi \left(\frac{\partial \boldsymbol{F}^p}{\partial \boldsymbol{U}} - \frac{1}{Re}\frac{\partial \boldsymbol{F}_v^p}{\partial \boldsymbol{U}}\right) + \phi^i \Delta t_s \delta_\eta \left(\frac{\partial \boldsymbol{G}^p}{\partial \boldsymbol{U}} - \frac{1}{Re}\frac{\partial \boldsymbol{G}_v^p}{\partial \boldsymbol{U}}\right)\right] \Delta \boldsymbol{U}$$
$$= -\phi^i \Delta t_s \left[J^{-1}\frac{(1+\phi)\boldsymbol{U}^p - (1+2\phi)\boldsymbol{U}^n + \phi \boldsymbol{U}^{n-1}}{\Delta t} + \boldsymbol{U}^p \frac{\partial J^{-1}}{\partial t} - \boldsymbol{U}^p \left[\frac{\partial J^{-1}}{\partial t} + \left(\frac{\xi_t}{J}\right)_\xi + \left(\frac{\eta_t}{J}\right)_\eta\right] + J^{-1}\delta_\xi \left(\boldsymbol{F}^p - \frac{1}{Re}\boldsymbol{F}_v^p\right) + J^{-1}\delta_\eta \left(\boldsymbol{G}^p - \frac{1}{Re}\boldsymbol{G}_v^p\right)\right] \tag{29}$$

where

$$\phi^i = 1/(1+\phi), \qquad \Delta \boldsymbol{U} = \boldsymbol{U}^{p+1} - \boldsymbol{U}^p \tag{30}$$

and for $p = 1$, $\boldsymbol{U}^p = \boldsymbol{U}^n$. One can see that on the RHS there is a cancellation of the $\partial J^{-1}/\partial t$ term that is accounted for in the following approximately factored numerical form:

$$\left[IJ^{-1} + \phi^i \Delta t_s \delta_\xi \left(\frac{\partial \boldsymbol{F}^p}{\partial \boldsymbol{U}} - \frac{1}{Re}\frac{\partial \boldsymbol{F}_v^p}{\partial \boldsymbol{U}}\right)\right] \times \left[IJ^{-1} + \phi^i \Delta t_s \delta_\eta \left(\frac{\partial \boldsymbol{G}^p}{\partial \boldsymbol{U}} - \frac{1}{Re}\frac{\partial \boldsymbol{G}_v^p}{\partial \boldsymbol{U}}\right)\right] \Delta \boldsymbol{U}$$
$$= -\phi^i \Delta t_s \left[J^{-1}\frac{(1+\phi)\boldsymbol{U}^p - (1+2\phi)\boldsymbol{U}^n + \phi \boldsymbol{U}^{n-1}}{\Delta t} - \boldsymbol{U}^p \left[\left(\frac{\xi_t}{J}\right)_\xi + \left(\frac{\eta_t}{J}\right)_\eta\right] + J^{-1}\delta_\xi \left(\boldsymbol{F}^p - \frac{1}{Re}\boldsymbol{F}_v^p\right) + J^{-1}\delta_\eta \left(\boldsymbol{G}^p - \frac{1}{Re}\boldsymbol{G}_v^p\right)\right] \tag{31}$$

Here, $\boldsymbol{U}^p$ is the subiteration approximation to $\boldsymbol{U}^{n+1}$, so that as $p \to \infty$, $\boldsymbol{U}^p \to \boldsymbol{U}^{n+1}$. It should be noted that with this subiteration approach the RHS of Eq. (31) represents the numerical approximation to the governing equation, whereas the left-hand side (LHS) vanishes as $p \to \infty$. The LHS then, may be modified without loss of formal accuracy, provided a sufficient number of subiterates is employed. In particular, a time step on the LHS of the equation Δt_s, may be chosen independently from the physical time step Δt on the RHS, thereby enhancing stability. Also the RHS of Eq. (31) can be modified to include a higher-order upwind algorithm, lagged boundary conditions, or lagged k-ε turbulence modeling without destroying the implicit nature of the algorithm. LHS efficiency improvements can also be implemented. The numerical procedure has been modified to include diagonalization, following the approach of Pulliam and Chaussee.[10] Although the diagonalized form of the ADI scheme is only first-order time-accurate and consistent with central differences, when coupled with subiterations, higher-order time accuracy may be recovered for a variety of discretization schemes. The diagonal form provides a 32% reduction in CPU time in two spatial dimensions relative to the block tridiagonal scheme. In three spatial dimensions the savings would be on the order of 50%. The numerical scheme [Eq. (31)] reverts to the standard first-order Beam-Warming procedure for $\phi = 0$, $\Delta t_s = \Delta t$, and $p = 1$.

In Eq. (31) all spatial derivatives are approximated by second-order-accurate central differences, and common forms of both implicit and explicit nonlinear dissipation[11] are employed to preserve numerical stability. The temporal metric derivatives are discretized in a manner consistent with the temporal derivative of the conserved variables in Eq. (31).

The subiteration implicit formulation can also be applied to the structural equations (26). The resulting scheme is

$$\left(I + \phi^i \Delta t_s \frac{\partial \boldsymbol{K}^p}{\partial \boldsymbol{S}}\right) \Delta \boldsymbol{S} = -\phi^i \Delta t_s \left[\frac{(1+\phi)\boldsymbol{S}^p - (1+2\phi)\boldsymbol{S}^n + \phi \boldsymbol{S}^{n-1}}{\Delta t} + \boldsymbol{K}^p\right] \tag{32}$$

Because the structural equations are cast in iterative form, as $p \to \infty$, a fully implicit coupling between the aerodynamic model and the structural model is obtained.

Grid-Deformation Approach

This research is ultimately targeted toward aeroelastic simulations of complex geometries in an overset grid context. For that application, simple moving grids would have the disadvantage of requiring that the overset grid connectivity be recalculated every time step. A preferred strategy is to allow grid deformation to accommodate aeroelastic deflection without motion of the grid overlap regions. Also, a deforming mesh allows for arbitrary deflection of aerodynamic control surfaces, and is not constrained to rigid body motion. An ideal methodology would be an efficient, algebraic method that maintains grid quality near the body, even under substantial, general deformation.

Of all the grid generation strategies available, trans-finite interpolation (TFI) is commonly used for aeroelastic applications. Some three-dimensional, unsteady aeroelastic solvers[1,2] use this simple, algebraic method to generate or to update the grid every time step. The method may consist of either connecting surfaces with straight lines in the body normal direction and preserving the arc-length distribution between nodes or a simple, linear distribution of translational displacements. The result is an algebraic grid that can accommodate simple surface deformations. However, grid quality may suffer for complex geometries or moderate deflections. In particular, mesh orthogonality at deforming surfaces, which is desired for high-Reynolds-number viscous flow simulation, is not guaranteed. In some cases, TFI can limit solution accuracy and stability,[12] suggesting the need for a more robust grid-deformation approach.

A grid deformation method that is suitable for aeroelastic simulations on overset grids was developed in the present work. This new strategy is similar to TFI in that it is an algebraic approach based on redefining the normal grid lines. However, unlike TFI, this method maintains the grid quality of the initial mesh near deforming surfaces under arbitrary, moderate deflections and rotations. In addition, a specified region in the far field may be held fixed so that the grid overlap regions and their connectivities remain unchanged.

The current grid-deforming algorithm is outlined here and illustrated in Fig. 2. Given a starting grid and a surface displacement, the translation and rotation of each surface node is

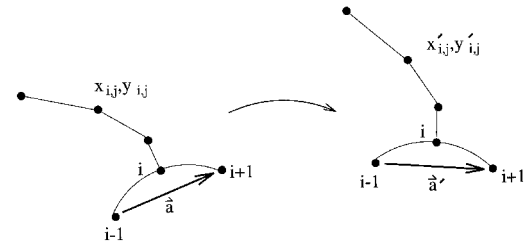

Fig. 2 Grid rotation.

computed from the deflected aerodynamic surface. The translational displacements are

$$\Delta x_i = x'_{i,1} - x_{i,1}, \qquad \Delta y_i = y'_{i,1} - y_{i,1} \tag{33}$$

whereas the rotational displacement can be expressed as

$$\cos\theta_i = \frac{\boldsymbol{a}\cdot\boldsymbol{a}'}{|\boldsymbol{a}||\boldsymbol{a}'|}, \qquad \sin\theta_i = \frac{(\boldsymbol{a}\times\boldsymbol{a}')\cdot\hat{e}_z}{|\boldsymbol{a}||\boldsymbol{a}'|} \tag{34}$$

where $\boldsymbol{a}$ is the original surface vector from $i-1$ to $i+1$ and $\boldsymbol{a}'$ is its displaced version. Each normal grid line is then moved in a rigid-body way according to the displacement of the surface node to form a reference, displaced grid line defined by

$$x^{\text{REF}}_{i,j} = x_{i,1} + \Delta x_i + (x_{i,j} - x_{i,1})\cos\theta_i - (y_{i,j} - y_{i,1})\sin\theta_i \tag{35}$$

$$y^{\text{REF}}_{i,j} = y_{i,1} + \Delta y_i + (x_{i,j} - x_{i,1})\sin\theta_i - (y_{i,j} - y_{i,1})\cos\theta_i \tag{36}$$

The new grid line is constructed by blending the reference grid line and the old grid line. The blending choice is arbitrary but is best done in arc-length space rather than in computational space. The arc-length for each node is defined

$$\tilde{s}_{i,j} = \sum_{k=2}^{j} \sqrt{(x_{i,k} - x_{i,k-1})^2 + (y_{i,k} - y_{i,k-1})^2} \tag{37}$$

where $\tilde{s}_{i,1} = 0$. A cubic blending with zero slope at the endpoints assures both that wall orthogonality is maintained and that the grid transitions smoothly in the far field. This can be written as

$$\tilde{b}_{i,j} = 3\left(\frac{\tilde{s}_{i,j}}{\tilde{s}_{i,j_{\max}}}\right)^2 - 2\left(\frac{\tilde{s}_{i,j}}{\tilde{s}_{i,j_{\max}}}\right)^3 \tag{38}$$

where $j_{\max}$ represents the last node along each normal line that is allowed to deflect. Finally, the new position of each grid point can be calculated by applying the blending function to the reference, displaced grid, and the original grid

$$\begin{aligned} x'_{i,j} &= \tilde{b}_{i,j}x_{i,j} + (1 - \tilde{b}_{i,j})x^{\text{REF}}_{i,j} \\ y'_{i,j} &= \tilde{b}_{i,j}y_{i,j} + (1 - \tilde{b}_{i,j})y^{\text{REF}}_{i,j} \end{aligned} \tag{39}$$

This method of grid deformation is used for all dynamic solutions presented in the following section.

Results

Results for the aeroelastic cylinder are presented in this section. Unless otherwise stated, dynamic solutions are computed employing the cubic blended grid-deformation strategy, the iterative block-tridiagonal form of the algorithm, and the GCL correction. Also, the LHS time step is equal to the RHS time step $\Delta t_s = \Delta t$ for all runs.

Static Cylinder

Static cylinder solutions were computed with freestream conditions corresponding to a Reynolds number of 5×10^2 and a Mach number of 0.2. Two grids were developed algebraically to investigate mesh resolution effects. The baseline grid had 384 evenly spaced points around the cylinder, and 96 points in the radial direction. A nondimensional spacing of 0.0005 was specified normal to the surface, and the grid was geometrically stretched to a maximum radius of 50 cylinder diameters. A finer grid was also used that had 772 and 192 points in the circumferential and normal directions, respectively. The far-field radius was held fixed at 50 diameters while the wall spacing was halved to 0.00025. Both grids were used to compute a shedding solution with a 0.005 time step, $\phi = \frac{1}{2}$, and $p_{\max} = 3$. The fine grid solution had a Strouhal number, peak lift coefficient, and mean drag coefficient of 0.224, 1.155, and 1.428, respectively. The corresponding values for the baseline grid solution were 0.229, 1.174, and 1.448. Thus, the baseline grid solution had a Strouhal number 2.2% lower, a peak C_l 1.6% higher, and a mean drag 1.4% higher than the corresponding results on the finer mesh. The observed reduction in Strouhal number with grid refinement was consistent with solutions presented by Alonso et al.[7] The relative insensitivity with a doubling of the grid dimensions gave confidence in the chosen baseline grid. Solutions presented hereafter were calculated with the baseline grid unless otherwise stated.

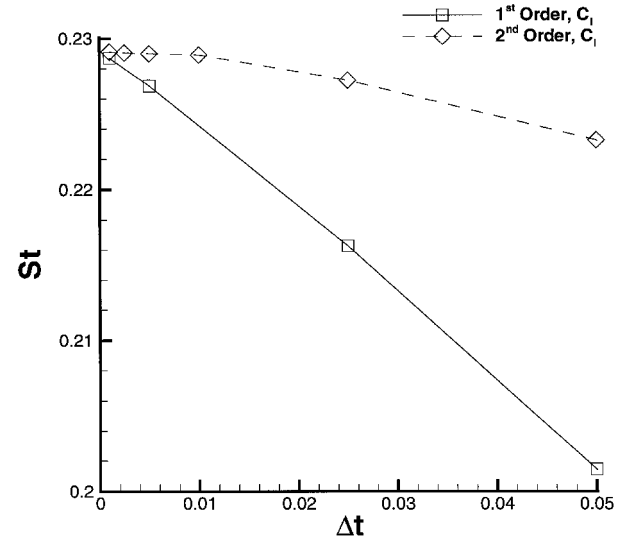

Fig. 3 Static cylinder time-step convergence ($Re = 5 \times 10^2$ and $M_\infty = 0.2$).

Time periodic solutions for a static cylinder were computed for various time steps. Once a time asymptotic solution was established, the nondimensional frequency of shedding St (measured from the variation in lift coefficient), the peak C_l, and the mean C_d were recorded. Figure 3 depicts the variation in St with a time step for $\phi = 0$ and $\frac{1}{2}$ and a maximum number of subiterates held fixed at $p_{\max} = 3$. First-order solutions ($\phi = 0$) converge to an asymptotic value in a linear manner, whereas second-order solutions ($\phi = \frac{1}{2}$) converge in a quadratic fashion. The second-order solution for $\Delta t = 0.025$ is nearly as accurate as the first-order 0.001 time-step solution. This implies that the second-order scheme allows a time step that is 10–25 times larger. Although the higher-order accurate scheme requires approximately two additional subiterations, a net workload improvement factor of 3–8 over the first-order standard scheme is still realized. It is also interesting to note that for a large time step of 0.05 the second-order solution differs only 3% from the asymptotic value, whereas the first-order solution displays a 10% difference. This indicates that a net workload improvement factor of 17, with only a 3% loss in accuracy, can be achieved.

Aeroelastic Cylinder

Free vibration solutions were computed to determine the characteristics of the fluid-structure interaction algorithm and they are presented in this section. Effects of varying numerical parameters associated with time integration, $p_{\max}$ and Δt, are investigated. The freestream conditions are the same as those of the previous section, $Re = 5 \times 10^2$ and $M_\infty = 0.2$. The baseline structural parameters used for all cases in this section are $\zeta = 1$, $\mu_s = 5$, and $\bar{u} = 4$.

A time-step convergence study was accomplished and presented in Fig. 4 for $\phi = 0$, $p_{\max} = 1$ and 3, and $\phi = \frac{1}{2}$, $p_{\max} = 3$. The results for $\phi = \frac{1}{2}$ produced a curve with quadratic behavior, implying the second-order accuracy of the coupled

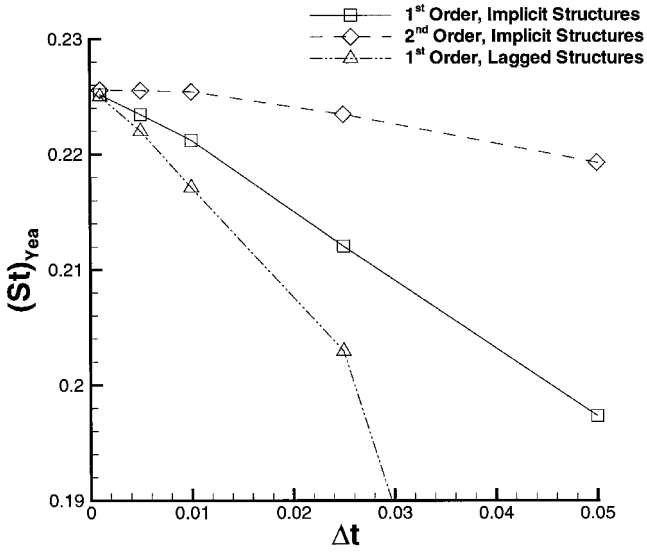

Fig. 4 Fluid-structure interaction time-step convergence (Re = 5 × 10², M_∞ = 0.2, ζ = 1, $\bar{u}$ = 4, and μ_s = 5).

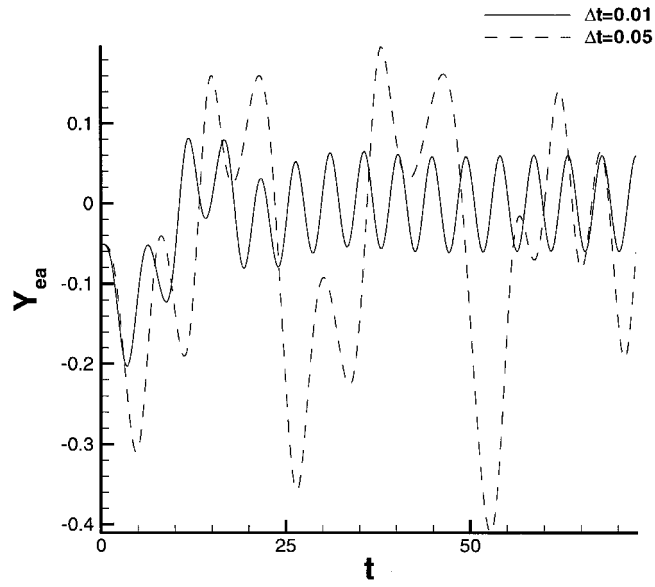

Fig. 5 Effect of large time steps on lagged structures (Re = 5 × 10², M_∞ = 0.2, ζ = 1, $\bar{u}$ = 4, and μ_s = 5).

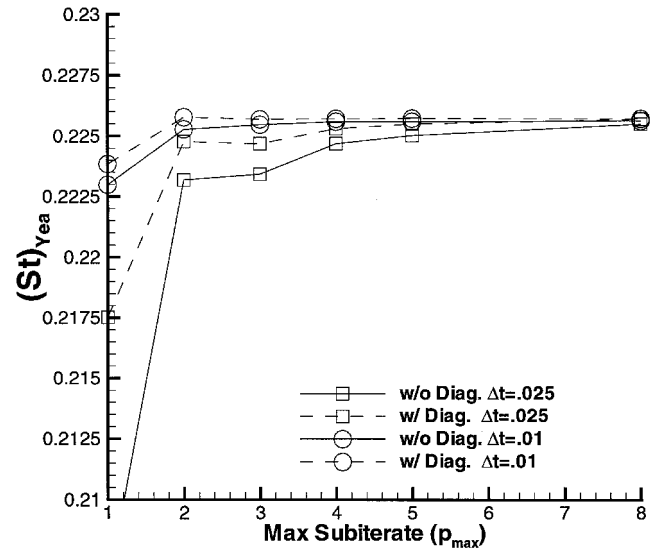

Fig. 6 Frequency of vertical motion for various max subiterates (Re = 5 × 10², M_∞ = 0.2, ζ = 1, $\bar{u}$ = 4, and μ_s = 5).

scheme. The three subiterations employed greatly reduced factorization and linearization error as well as lagging error between the fluid and structure time-integration schemes, allowing the coupled system to approach second-order accuracy. The Strouhal number for a 0.05 time-step solution was less than 3% lower than the asymptotic value of 0.2256 and the time histories of X_{ea}, Y_{ea}, C_l, and C_d were all sinusoidal with constant amplitude.

The first-order-coupled system produced a linear convergence curve with the same asymptotic Strouhal number of 0.2256. The Strouhal number for a time step of 0.05 was 0.198, 12.3% lower than the asymptotic value. As in the second-order solutions the time histories of X_{ea}, Y_{ea}, C_l, and C_d were all sinusoidal.

Comparison of the implicit coupling method to a traditional lagged structures method[1,2,12] was accomplished by removing the structural solver from the subiteration loop, setting $\phi = 0$ and $p_{max} = 1$. The convergence curve is also depicted in Fig. 4. First-order accuracy is evident from the linear behavior of the curve. The increase in slope of the lagged structures convergence curve was attributed to the linearization, factorization, and lagging errors not eliminated through subiteration. A comparison between the second-order-coupled scheme and the lagged structures scheme implies that a factor of 10–20 in time step over traditional methods can be realized with virtually no degradation in solution accuracy.

Another important finding is the drastic change in the qualitative nature of the lagged approach for time steps greater than 0.025. Figure 5 shows time histories of Y_{ea} for two time steps using the lagged structures approach. The 0.01 time-step solution is time periodic with a single amplitude and frequency, whereas the 0.05 time-step solution is not. This behavior persisted for an additional 150 characteristic time units and is even more chaotic as the time step increases. In contrast, the fully implicit method preserves the qualitative behavior for very large time steps.

In the previous results, the maximum number of subiterations was held fixed while the time step was varied. Figures 6 and 7 depict the change in solution behavior as p_{max} is increased and the time step is held constant. Solutions are presented for both the block-tridiagonal and the diagonal schemes for two different time steps, 0.01 and 0.025. As p_{max} is increased from one to eight, all solutions converged to within 0.05% of the asymptotic value, St = 0.2256 (Fig. 4). This implies that linearization, factorization, and lagging structures errors dominate the temporal truncation error and can be eliminated with subiteration. The p_{max} = 3 solution differs only by 1% from the asymptotic solution, validating this choice of p_{max} for the remaining runs. The noniterative Beam–Warming solution ($\phi = \frac{1}{2}$, p_{max} = 1) for the time step of 0.025 is over 9% lower than the asymptotic solution, demonstrating the inaccuracy introduced when using these large time steps with the standard method.

It is interesting to note that the diagonalized scheme converges to the asymptotic value in fewer subiterations than the block-tridiagonal form. This can be attributed to the fact that the diagonal version utilizes a scalar pentadiagonal solver, maintaining the full dissipation stencil for the implicit term, whereas in the block-tridiagonal solver a truncated implicit dissipation stencil is employed. Solutions obtained with the diagonalized form for the two different time steps are essentially converged (<0.5%) for p_{max} = 2.

Numerical and Experimental Comparison

This section presents results for the free vibration conditions matching experiments and numerical simulations of other researchers.[5–7] This comparison is intended to give overall confidence in the developed method through cross validation. The

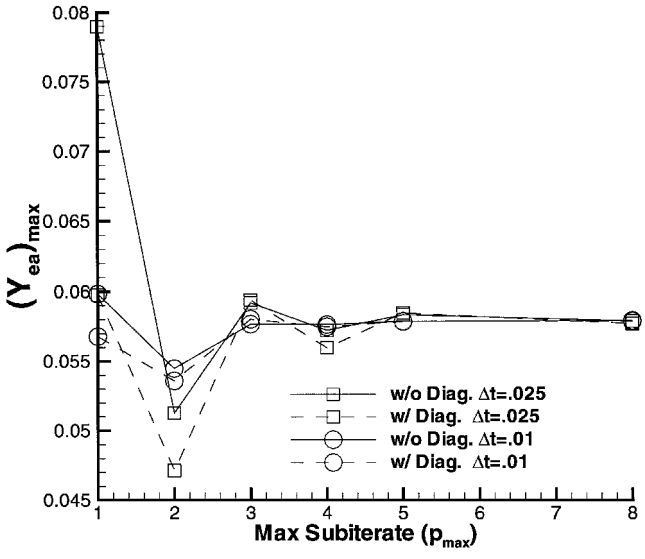

Fig. 7 Amplitude variation for various max subiterates (Re = 5 × 10^2, M_∞ = 0.2, ζ = 1, $\bar{u}$ = 4, and μ_s = 5).

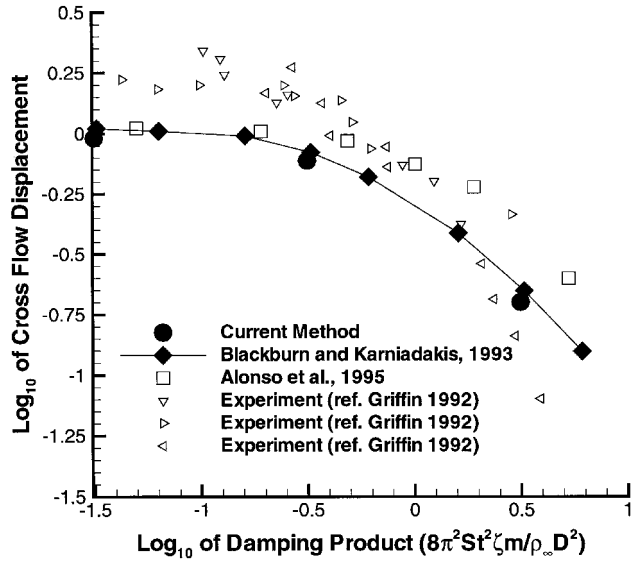

Fig. 8 Experimental and numerical comparison of maximum crossflow displacement.

numerical simulations of Blackburn and Karniadakis[5] are computed with an incompressible spectral method at a Reynolds number of 2 × 10^2. Alonso et al.[7] used a third-order temporal and second-order spatial implicit algorithm to compute solutions at a Reynolds number of 5 × 10^2 and a freestream Mach number of 0.2. In the current work solutions were computed with the baseline grid and the new mesh deformation strategy for a Reynolds number of 2 × 10^2 and a freestream Mach number of 0.1.

Comparison data were for conditions of locking or frequency coalescence. This is a condition whereby the aerodynamic shedding frequency and the mechanical system frequency coalesce producing a similar system response frequency. To determine the proper mechanical system frequency, a static cylinder solution was computed for Re = 2 × 10^2, M_∞ = 0.1 with a time step of 0.005, and p_{max} = 2. The resulting Strouhal number was 0.1997. The spring stiffness was then tuned to match spring natural frequency and shedding frequency with the relationship

$$2/\bar{u} = 2\pi St \tag{40}$$

producing a reduced velocity $\bar{u} = 1/\pi St = 1.5939$. All three comparison runs were for $m/\rho D^2 = 10$, allowing direct comparison with Blackburn and Karniadakis,[5] resulting in $\mu_s = 40/\pi = 12.73$. Three damping ratios ζ were used to directly compare with the damping product of Blackburn and Karniadakis,[5] ζ = 0.001, 0.01, and 0.1. The damping product is defined as $8\pi^2St^2\zeta(m/\rho D^2)$, where the Strouhal number used in this relationship was 0.1997.

Figure 8 displays the agreement between the experiments and numerical simulation. Comparison data[5,7] were digitized from hard-copy figures. The abscissa is the damping product and the ordinate is twice the amplitude of motion nondimensionalized by the diameter of the cylinder. All three numerical methods were in close agreement in the amplitude limiting region of a low damping product. Good agreement was observed between the current method results and those of Blackburn and Karniadakis[5] for the complete range of damping products. The solutions of Alonso et al.[7] predicted higher crossflow displacements for the higher damping product solutions that may be attributed to the higher Reynolds number employed. The three-dimensional experimental data compare qualitatively to the current method through the complete range of damping products.

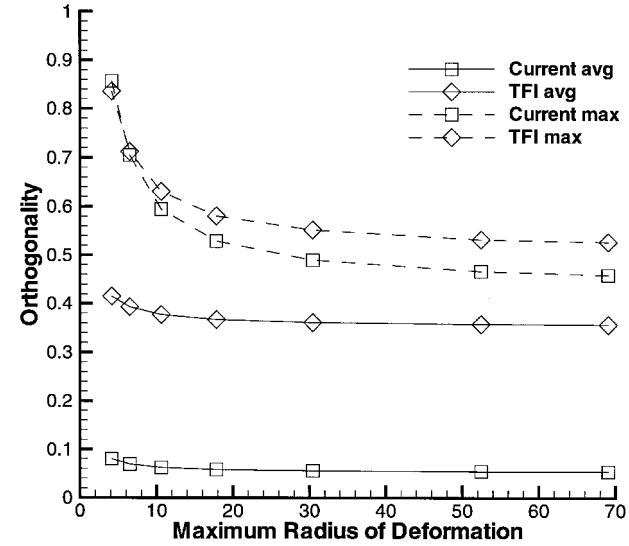

Fig. 9 Grid orthogonality for three grid-deforming methods.

Grid-Deformation Effects

To illustrate the effect of the current grid-deformation strategy, an assessment of grid quality under deformation is presented. The grid is a polar O-grid about a circular cylinder of unit diameter. There are 200 points in the circumferential direction and 100 in the normal direction, with an initial wall spacing of 0.00001. The cylinder is given a translational displacement of one diameter and a 28-deg rotation and then a new grid is obtained. The grid was allowed to deform only up to a specified location away from the cylinder to simulate the frozen far field required for overset grids.

This displaced cylinder case was run using both TFI and the present cubic blended method. For the purposes of this study the TFI method was represented with the current algorithm by substituting a linear, arc-length-based blending function and by holding the surface rotation angles to zero. The deformed grid quality was assessed by computing the grid orthogonality (or cosine of the angle formed by intersecting grid lines). The distance of the fixed boundary was varied to assess the effect of grid slack (grid available to accommodate deformation) on the mesh quality. Grid orthogonality as a function of radius of deformation is plotted in Fig. 9. In terms of both the maximum and average values, the current (cubic) method produced grids

that were more orthogonal than TFI. For the most extreme cases, the maximum loss of orthogonality was comparable, whereas the average values favored the current method. Also, the TFI method exhibited nearly uniform skewness while the current method maintained orthogonality at the wall.

Overall, the current grid-deforming strategy proved to be promising for application on overset grids. It provides a mechanism for preserving grid quality under moderate translational and rotational deformations, particularly at the surface. Finally, the calculation is algebraic and simple and extends readily to three dimensions.

Geometric Conservation Law Effects

In this section the effect of including the GCL term in the governing equations is assessed. The grid described in the preceding section was used to analyze freestream preservation. Freestream conditions were imposed on both the surface and outer boundaries and the surface was rotated 1 rad and returned in one characteristic time unit. The mesh was deformed at each time step employing the new grid-deformation strategy. A time step of 0.05 was used with $p_{\max} = 3$ and $\phi = \frac{1}{2}$ (second order).

The simulation produced an average error norm in total energy equal to 3.9×10^{-4} without GCL correction and 2.7×10^{-15} with GCL correction. This implies that without GCL correction an error orders of magnitude larger than single precision is introduced. Using the GCL correction term of Eq. (3) eliminates the error to double-precision accuracy.

A similar comparison was accomplished for the elastically mounted cylinder but the solutions agreed to within plotting accuracy. Although the correction did not make dramatic improvements to the aeroelastic cylinder calculation, it is more representative of the governing equations and is easily implementable. Implementing the GCL correction term may make the algorithm more robust for large translational and rotational deformations.

Summary and Conclusions

A fully implicit iterative fluid-structure interaction algorithm was developed, and issues of efficiency and accuracy were examined. Coupling the structures into the subiteration loop produced an overall scheme that was second-order accurate in time, allowing an order of magnitude increase in time step over the standard lagged structures approach, which translates to a significant workload reduction. An additional benefit of the subiteration approach was the ability to use the more efficient diagonalized form while maintaining higher-order time-accuracy.

A new algebraic grid-deformation strategy, applicable to overset grids, was developed that preserves grid orthogonality near the body for significant deformations. Geometric conservation corrections preserved freestream to machine accuracy for severe grid deformations, improving the accuracy of dynamic grid computations.

Finally, the overall approach accurately captured the aeroelastic response of an elastically mounted cylinder as evidenced by favorable comparison with previous experiments and computations.

Acknowledgments

This work was sponsored by the U.S. Air Force Office of Scientific Research under Task 2307 AW, monitored by L. Sakell. Juan Alonso of Princeton University and Karniadakis of Brown University proved instrumental in the comparison with experimental and numerical solutions. This work was supported in part by a grant of HPC time from the DoD HPC Shared Resource Center ASC at Wright–Patterson Air Force Base, Ohio.

References

[1]Smith, M. J., Schuster, D. M., Huttsell, L., and Buxton, B., "Development of an Euler/Navier-Stokes Aeroelastic Method for Three-Dimensional Vehicles with Multiple Flexible Surfaces," *Proceedings of the AIAA/ASME/ASCE/AHS/ASC 37th Structures, Structural Dynamics, and Materials Conference* (Salt Lake City, UT), AIAA, Washington, DC, 1996.

[2]Guruswamy, G. P., "Unsteady Aerodynamic and Aeroelastic Calculations for Wings Using Euler Equations," *AIAA Journal*, Vol. 28, No. 3, 1990, pp. 461–469.

[3]Morton, S. A., and Beran, P. S., "Nonlinear Analysis of Airfoil Flutter at Transonic Speeds," AIAA Paper 95-1905, June 1995.

[4]Rizzetta, D. P., and Visbal, M. R., "Comparative Numerical Study of Two Turbulence Models for Airfoil Static and Dynamic Stall," *AIAA Journal*, Vol. 31, No. 4, 1993, pp. 784–786.

[5]Blackburn, H. M., and Karniadakis, G. E., "Two- and Three-Dimensional Vortex-Induced Vibration of a Circular Cylinder," *Proceedings of the International Society of Offshore and Polar Engineers (ISOPE) 93 Conference*, Vol. 3 (Singapore), 1993, pp. 715–720.

[6]Griffin, O. M., "Vortex Induced Vibrations of Marine Structures in Uniform and Sheared Currents," National Science Foundation Workshop on Riser Dynamics, Univ. of Michigan, Ann Arbor, MI, 1992.

[7]Alonso, J., Martinelli, L., and Jameson, A., "Multigrid Unsteady Navier-Stokes Calculations with Aeroelastic Applications," AIAA Paper 95-0048, Jan. 1995.

[8]Thomas, P. D., and Lombard, C. K., "Geometric Conservation Law and Its Application to Flow Computations on Moving Grids," *AIAA Journal*, Vol. 17, No. 10, 1979, pp. 1030–1037.

[9]Beam, R., and Warming, R., "An Implicit Factored Scheme for the Compressible Navier-Stokes Equations," *AIAA Journal*, Vol. 16, No. 4, 1978, pp. 393–402.

[10]Pulliam, T. H., and Chaussee, D. S., "A Diagonal Form of an Implicit Approximate-Factorization Algorithm," *Journal of Computational Physics*, Vol. 39, No. 2, 1981, pp. 347–363.

[11]Jameson, A., Schmidt, W., and Turkel, E., "Numerical Solutions of the Euler Equations by Finite Volume Methods Using Runge-Kutta Time Stepping Schemes," AIAA Paper 81-1259, June 1981.

[12]Farhangnia, M., Guruswamy, G., and Biringen, S., "Transonic-Buffet Associated Aeroelasticity of a Supercritical Wing," AIAA Paper 96-0286, Jan. 1996.